The Modeling of a Laboratory Natural Gas-Fired Furnace with a Higher-Order Projection Method for Unsteady Combustion*

R.B. Pember, P. Colella, L.H. Howell, A.S. Almgren,
J.B. Bell, W.Y. Crutchfield, V.E. Beckner
Lawrence Livermore National Laboratory
K.C. Kaufman, W.A. Fiveland, and J.P. Jessee
Babcock & Wilcox Research and Development Division

ABSTRACT

A higher-order, embedded boundary projection method for axisymmetric, unsteady, low-Mach number combustion is used to model a natural gas flame from a 300kW IFRF burner in the Burner Engineering Research Laboratory (BERL) at Sandia National Laboratory under hot wall conditions. The numerical predictions presented are the late simulated-time results of a computation of unsteady flow in the furnace. The predictions are compared both with measurements completed in the BERL as part of the GRI SCALING 400 Project and with results from a steady-state axisymmetric reacting flow code in order to evaluate the combustion model and the numerical method. The results compare favorably with the experimental data.

1 INTRODUCTION

The ability to model transient effects in furnaces is becoming increasingly important. The problem of ensuring the safe performance of an industrial furnace, for example, is more difficult during the startup or shutdown phases of operation than during normal operating conditions. The peak formation of pollutants is more dependent on transient behavior, in particular, on peak temperatures, than on average operating conditions. The failure to establish a stable flow can only be addressed with an unsteady method.

In this paper, we validate the methodology of Pember et al. [1] by using it to simulate a natural gas flame from a 300kW IFRF burner in the Burner Engineering Research Laboratory (BERL) at Sandia National Laboratory under hot wall conditions. The algorithm is a higher-order projection method that computes unsteady, low-Mach number axisymmetric reacting flow on a uniform rectangular grid with embedded boundaries. The numerical predictions presented are the late simulated-time results from a computation of time-dependent flow in the furnace. The results are compared both with measurements completed in the BERL as part of the GRI SCALING 400 Project [2] and with the predictions of Kaufman and Fiveland [3] using the steady-state axisymmetric flow method of Jessee and Fiveland [4]. The comparisons are used to evaluate the combustion model and the numerical method.

*This work was performed under the auspices of the U.S. Department of Energy by the Lawrence Livermore National Laboratory under contract W-7405-Eng-48. Support under contract W-7405-Eng-48 was provided by the Applied Mathematical Sciences Program and the HPCC Grand Challenge Program of the Office of Scientific Computing at DOE. Kaufman, Fiveland, and Jessee acknowledge Dr. R.V. Serauskas and the Gas Research Institute Basic Research Group for support of their work through GRI contract 5093-260-2729.

The main goal of this work is to evaluate the use of a low-Mach number model for combustion [5, 6] and a higher-order projection methodology in a simulation of a natural gas-fired furnace. As such, we assume that the perfect gas law applies. We also use several relatively simple, standard submodels, namely, a two-step reduced kinetics mechanism [7], a $k-\epsilon$ model for turbulent transport [8], and an eddy-dissipation model for turbulent combustion [9]. GRI-Mech data [10] and simple polynomial correlations [2] are used to compute thermochemical properties and laminar diffusivities.

Our method is based on a higher-order projection method for incompressible flow [11, 12] and uses a sequential formulation. Hence, it is qualitatively similar to SIMPLE [13].

2 MATHEMATICAL MODEL

For a multi-component perfect gas in a low-Mach number ($M < .3$) axisymmetric flow, the following constraint on the divergence of the velocity is effectively satisfied [5, 6]:

$$\nabla \cdot (u, v)^T = \frac{1}{T}\frac{DT}{Dt} + mw_{mix} \sum_l \frac{1}{mw_l}\frac{Dm_l}{Dt}. \tag{1}$$

The governing differential equations consist of the divergence constraint (1) and the following evolution equations for density, velocity, enthalpy, temperature, species mass fractions, and turbulent kinetic energy and dissipation rate:

$$\frac{\partial \rho}{\partial t} + \nabla \cdot \rho U = 0 \tag{2}$$

$$\frac{\partial \rho\,(u,\ v,\ w)^T}{\partial t} + (\nabla \cdot \rho U u,\ \nabla \cdot \rho U v,\ \nabla \cdot \rho U w)^T + \left(-\frac{\rho w^2}{r},\ \rho g,\ \frac{\rho u w}{r}\right)^T = -\nabla \pi + \nabla \cdot \tau \tag{3}$$

$$\frac{\partial \rho h}{\partial t} + \nabla \cdot \rho U h \quad = \quad \nabla \cdot \lambda_e \nabla T - \nabla \cdot q_{rad} + \nabla \cdot \textstyle\sum_l \rho h_l(T) D_e \nabla m_l \tag{4}$$

$$\rho c_p \frac{DT}{Dt} = \nabla \cdot \lambda_e \nabla T - \nabla \cdot q_{rad} + \nabla \cdot \sum_l \rho h_l(T) D_e \nabla m_l - \rho \sum_l \frac{Dm_l}{Dt} h_l(T) \tag{5}$$

$$\frac{\partial \rho m_l}{\partial t} + \nabla \cdot \rho U m_l = \nabla \cdot D_e \rho \nabla m_l - R_l \tag{6}$$

$$\frac{\partial \rho k}{\partial t} + \nabla \cdot \rho U k = \nabla \cdot \left(\frac{\mu_t}{\sigma_k} + \mu\right) \nabla k - R_{ij}\frac{\partial U_i}{\partial x_j} - \rho \epsilon \tag{7}$$

$$\frac{\partial \rho \epsilon}{\partial t} + \nabla \cdot \rho U \epsilon = \nabla \cdot \left(\frac{\mu_t}{\sigma_\epsilon} + \mu\right) \nabla \epsilon - C_1 \frac{\epsilon}{k} R_{ij}\frac{\partial U_i}{\partial x_j} - C_2 \rho \frac{\epsilon^2}{k} \tag{8}$$

The right hand sides of (5) and (6) are used to evaluate DT/Dt and Dm_l/Dt in (1). The standard values of the $k-\epsilon$ model constants are used, and the effective diffusivities μ_e, λ_e, and D_e are defined in the usual way [8].

The enthalpy h is defined by

$$h = \sum_l m_l h_l(T), \tag{9}$$

where $h_l(T)$, the specific enthalpy of species l, includes the heat-of-formation of l. When needed, T is computed using h, m_l, and (9); equation (5) is used only in evaluating (1).

In equation (6), R_l represents the mass rate of consumption of species l. In this paper, the following two-step reaction model for methane oxidation [7] is used:

$$\begin{aligned} CH_4 + {}^3\!/\!_2 O_2 &\rightarrow CO + 2H_2O \\ CO + {}^1\!/\!_2 O_2 &\rightarrow CO_2. \end{aligned} \tag{10}$$

The corresponding rate of each reaction is the smaller of two rates, the first given by the Arrhenius rate equation recommended in [7] and the second by an eddy-dissipation model [9], respectively. The composition of the fluid is modeled with the five species shown in (10) and N_2. Note that CO_2 disassociation is neglected.

2.1 Boundary Conditions

We use recommended [8, 14] inlet values for k and ϵ. At solid walls, the "law-of-the-wall" [8, 14] is used to compute ϵ, τ, and the conductive heat flux at the wall.

3 NUMERICAL ALGORITHM

The algorithm used in advancing the solution a single time step from time t^n to $t^n + \Delta t = t^{n+1}$ is described in [1] and summarized below.

We use a uniform grid (Fig. 1 of rectangular cells with widths Δr and Δz indexed by i and j. The center of cell ij is $((i+.5)\Delta r, (j+.5)\Delta z)$. The index ij is used to denote a value centered in cell ij or, equivalently, an average value over the cell. The upper, right corner of cell ij is denoted by the index $(i + {}^1\!/\!_2, j + {}^1\!/\!_2)$. At the beginning of the time step, the numerical solution, except for pressure, represents the flow at time t^n at cell centers. The solution for pressure, $\pi^{n-1/2}_{i+1/2,j+1/2}$, represents the pressure at the previous half-time step, $t^{n-1/2}$, on cell corners.

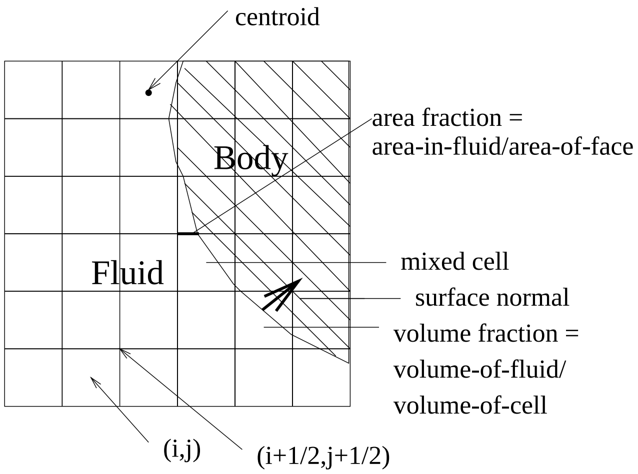

Figure 1: Embedded boundary representation of geometry in two-dimensional cells. Additional integrated quantities are required by the solution of the elliptic equation used to impose the divergence constraint.

The furnace wall is represented as a boundary embedded in a uniform, rectangular grid. Hence, the fluid domain consists of uniform rectangular cells except at the furnace wall where irregular (mixed) cells may be present. The boundary is essentially described by volume and area fractions (Fig. 1). The volume fraction Λ_{ij} is the fraction of the volume of cell ij that contains fluid. The numerical solution is defined on all cells for which $\Lambda_{ij} > 0$. Due to the finite element formulation of the projection [15], the pressure solution is defined on all four corners of these cells.

The method is a predictor-corrector scheme. In the predictor step, values of k, ϵ, w, h, and m_l are computed at time t^{n+1} using explicit higher-order upwind differencing [11, 12] of the convective terms and Crank-Nicholson differencing of the diffusive and the reactive terms. In addition, values of U, denoted by U^* or (u^*, v^*), are computed in this step which do not necessarily satisfy the divergence constraint (1) at t^{n+1}. In the corrector step, the divergence constraint is imposed on the velocity through the solution of an elliptic equation, yielding U^{n+1} and $\pi^{n+1/2}_{i+1/2,j+1/2}$, the pressure at $t^{n+1/2} = t^n + \Delta t/2$. The time step Δt used to advance the solution satisfies the Courant-Friedrichs-Lewy (CFL) condition for the stability of the explicit upwind scheme,

$$\Delta t = \sigma \min_{ij:\Lambda_{ij}>0} \left(\frac{\Delta r}{u^n_{ij}}, \frac{\Delta z}{v^n_{ij}} \right) \tag{11}$$

where the CFL number σ satisfies $\sigma < 1$.

The predictor step of the algorithm consists of the following steps:

(I) Compute discrete approximations of the convective terms in the governing equations at time $t^n + \Delta t/2$ using the embedded boundary convective differencing techniques in [15]:

$(\nabla \cdot \rho U \varphi)^{n+1/2}_{ij}$ for $\varphi = h, m_l, w, k, \epsilon$ and
$(U \cdot \nabla \varphi)^{n+1/2}_{ij}$ for $\varphi = u, v$.

(II) Compute $\rho^{n+1}_{ij} = \rho^n_{ij} - \Delta t \sum_l (\nabla \cdot \rho U m_l)^{n+1/2}_{ij}$.

(III) Predict values of $k, \epsilon, m_l, h, u^*, v^*$, and w at t^{n+1} using the Crank-Nicholson method.

(IV) Use a discrete ordinates method [16, 17, 18] to compute $(\nabla \cdot q_{rad})^{n+1}$ using values of T computed from the values of h and m_l found in (III).

(V) Correct the values of all the flow quantities to provide the solution at time t^{n+1}, again using Crank-Nicholson differencing.

In steps (III) and (V) the evolution equations for the flow quantities are solved sequentially so that only linear systems of equations result from the Crank-Nicholson differencing. The linear systems are solved with a multigrid accelerated Gauss-Seidel scheme [19]. The Crank-Nicholson method is applied twice for each evolution equation in order to obtain time-centered values for second-order accuracy. The equations used to advance u and v are the non-conservative form of the first two rows of equation (3). The update for species is itself performed sequentially in two steps, one accounting for convection and diffusion and the other for kinetics. In step (III), we use a diamond-difference discrete-ordinates model similar to those presented in [16, 17, 18], modified to include the appropriate emitting, reflecting, and absorbing boundary conditions along the embedded boundary.

In the corrector, an approximate projection [12, 15] is used to enforce the divergence constraint (1) and determine $\pi^{n+1/2}$. The equation

$$\nabla \cdot \left(\frac{1}{\rho^{n+1/2}_{ij}} (\nabla \delta)_{ij} \right) = \nabla \cdot \left(\frac{U^{*,n+1}_{ij} - U^n_{ij}}{\Delta t} \right) - \frac{S^{n+1}_{ij} - S^n_{ij}}{\Delta t}, \tag{12}$$

is solved using a standard finite-element bilinear discretization. S equals the right hand side of equation (1) plus additional terms accounting for the fact that the perfect gas law and equations

(2), (4), (6), and (9) represent an overdetermined set of equations for ρ. U^{n+1} and $\pi^{n+1/2}$ are then found by

$$\begin{aligned} U_{ij}^{n+1} &= U_{ij}^{*,n+1} - \frac{\Delta t}{\rho_{ij}^{n+1/2}} \left(\bar{G}\delta\right)_{ij} \\ \pi_{i+1/2,j+1/2}^{n+1/2} &= \pi_{i+1/2,j+1/2}^{n-1/2} + \delta_{i+1/2,j+1/2} \end{aligned} \tag{13}$$

where $\left(\bar{G}\delta\right)_{ij}$ represents the cell average of $\nabla\delta$ over cell ij.

4 FURNACE AND BURNER DESCRIPTION

4.1 Background

The Gas Research Institute has funded work, under GRI contract 5093-260-2729, to produce a document that can be used by model developers to validate natural gas combustion codes. Initial combustion tests were completed in the Burner Engineering Research Laboratory (BERL), located at Sandia National Laboratories (SNL) in 1994 [20]. These measurements were used as the baseline set for the initial validation document released in November, 1994 [2].

4.2 Description

The furnace geometry is shown in Fig. 2. The furnace is vertically-fired consisting of a base plate (in which the burner is installed), five octagonal "spool" sections, and a conical furnace hood with a cylindrical exhaust duct. The spool sections were constructed using refractory-lined panels for the hot-wall measurements. The furnace base, hood, and exhaust duct are lined with insulating board. Initial tests included six traverses at .027, .109, .177, .191, .343, and .432m downstream of the burner throat, as well as the furnace exit conditions 2.794m downstream of the throat.

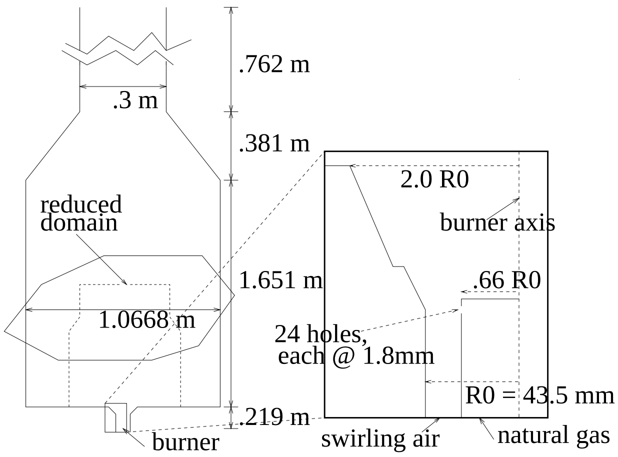

Figure 2: Sketches of the BERL furnace and the IFRF 300kW gas burner. The reduced computational domain used in the bootstrapping procedure is also sketched.

The gas burner geometry is sketched in Fig. 2. The 300kW burner is a swirl-stabilized natural gas burner which is circumferentially symmetric with a bluff centerbody containing 24 radial natural gas injection holes. Combustion air is introduced through one annular zone and swirled using IFRF swirl blocks. Neither flue gas recirculation nor natural gas staging are considered.

4.3 Inlet and wall conditions

Natural gas enters at 22.7 kg/hr at 308.15° K, while air at 312.15° K enters the burner at 31.35 m/sec (15% excess air) with a swirl number of .56. The wall temperature conditions and other details are described in [2, 3].

5 COMPUTATIONAL STRATEGY

5.1 Approximations

The furnace chamber is considered to be cylindrical with a radius of .5334m. The 24 gas injection holes are modeled as an annular slot. The height of the slot equals that of one computational cell (Δz). The fuel inlet conditions are approximated by matching the mass flow rate. Natural gas is approximated by a $CH_4 - CO_2 - N_2$ mixture and air by a $O_2 - N_2$ mixture [2, 3]. The furnace walls are assumed to have time-independent temperature profiles.

5.2 Gridding

The computational domain contains only the first .19m of the exhaust duct. The domain is covered by a uniform 96×448 rectangular grid, i.e., $\Delta r = \Delta z = .00556$m. The description of the furnace wall in the embedded boundary formulation was computed following the guidelines in [15, 21].

5.3 Initial conditions

The computational domain is filled with air at 312.15° K except for a small patch just outside the burner throat at 2000° K which serves as an ignition source. u and v satisfy equation (1) for the given interior and inlet conditions. k and ϵ are set to small values.

5.4 Bootstrapping procedure

We used a "bootstrapping" procedure in order to accelerate the solution toward steady state. A reacting flow solution was first computed on a reduced 48×192 grid with the same cell widths as the full grid, corresponding to the same burner geometry but a smaller furnace geometry (Fig. 1). After 5000 time steps, this solution was lifted into the full 96×448 grid. The solution was copied where the fluid domains of the two grids overlapped and was then extended to the remainder of the full grid. The lifted velocity field was projected [11, 12] so that it satisfied the divergence constraint (1). The lifted solution was then used as the initial data for a computation on the full grid of an additional 34500 time steps.

Time step 39500 corresponds to a simulated time of 3.8 sec; however, the computed results cannot truly be considered a calculation of the time dependent flow because of the "bootstrapping" procedure.

6 COMPUTATIONAL RESULTS

The numerical results at time step 39500 are shown in Fig. 3 - 6. The axial velocity and the temperature fields are shown in Fig. 3. Computed radial profiles (at .027m and .343m downstream of the burner throat) and the computed centerline profiles of axial and tangential components of velocity, temperature, and mole fractions of O_2, CO_2, and CO are compared in Fig. 4 - 6. with experimental data [2]. Steady-state predictions [4, 3] are included for further comparison.

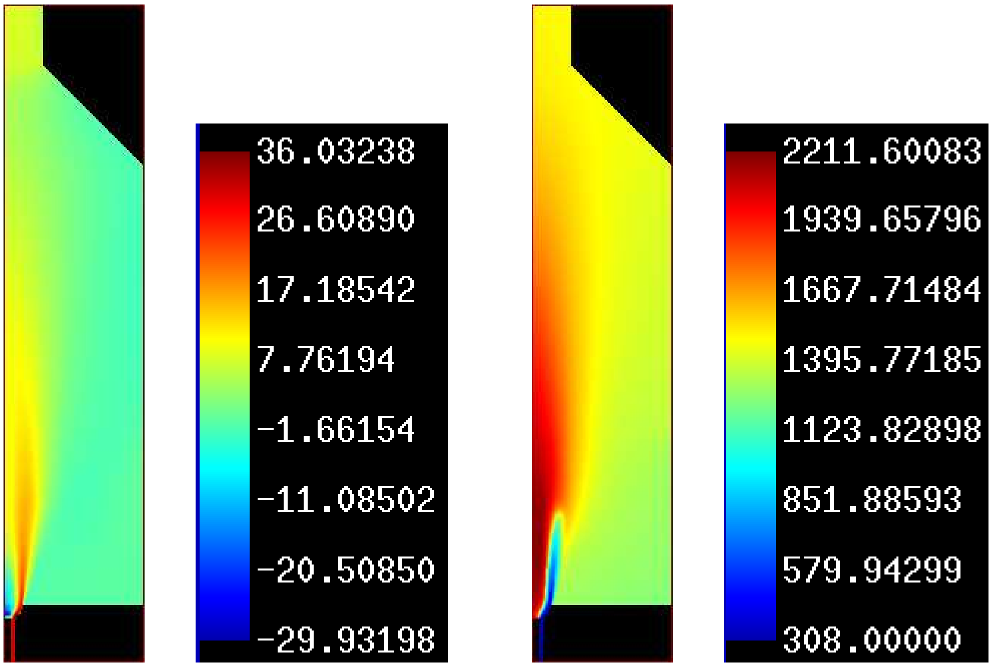

Figure 3: Computed axial velocity and temperature fields at time step 39500.

The comparisons with experimental data are generally favorable. There are some noticeable discrepancies, however.

In the region near the burner throat, the computed temperatures exceed the measured values along the centerline but dip noticeably below the measurements just off the centerline. This trend is observed in the radial profiles at .027m and .343m. The measurements display a similar trend at .027m, but not at .343m. There are similar differences at .343m between the computed and the measured O_2 and CO_2 concentrations. The discrepancies between the steady-state predictions and the experimental data display similar trends. The differences between the two sets of computed values and the measurements are most likely due to the assumption of cylindrical symmetry, and, in particular, the approximation of the flow inlet as an annular slot. Both the unsteady and the steady-state axisymmetric codes model the fuel jet as a structure roughly like a conical frustum. The elongation of the fuel jet and the higher temperatures in the internal recirculation zone in the computed solutions may be due to the lack of the three-dimensional dissipation mechanisms which accelerate both the dissolution of the 24 gas jets and the dissipation of heat away from the flame front in the actual flow. We note that another explanation of the high temperatures in the IRZ is the use of a reduced mechanism. Specifically, the adiabatic flame temperature of a CH_4-air flame without dissociation is roughly 100° K higher than an actual natural gas-air flame [22]. A third explanation applicable only to the unsteady method is that the effective Lewis number of the simulated flow is not unity because of the nonlinearity of the higher-order upwind scheme.

Nearer to the furnace wall, the predicted O_2 and CO_2 concentrations are greater and less than the measurements, respectively. Time dependent results (Fig. 7) show that the numerical solution at step 39500 has not reached steady state and that the concentrations of O_2 and CO_2 are tending toward the measured values as the calculation progresses.

CO concentrations are overpredicted at .343m. A possible explanation for this disagreement is that our implementation of the eddy dissipation model [9] uses the same rate constant (4.0) in both the CH_4 and the CO oxidation steps. Hence, the different rates of the two reactions when

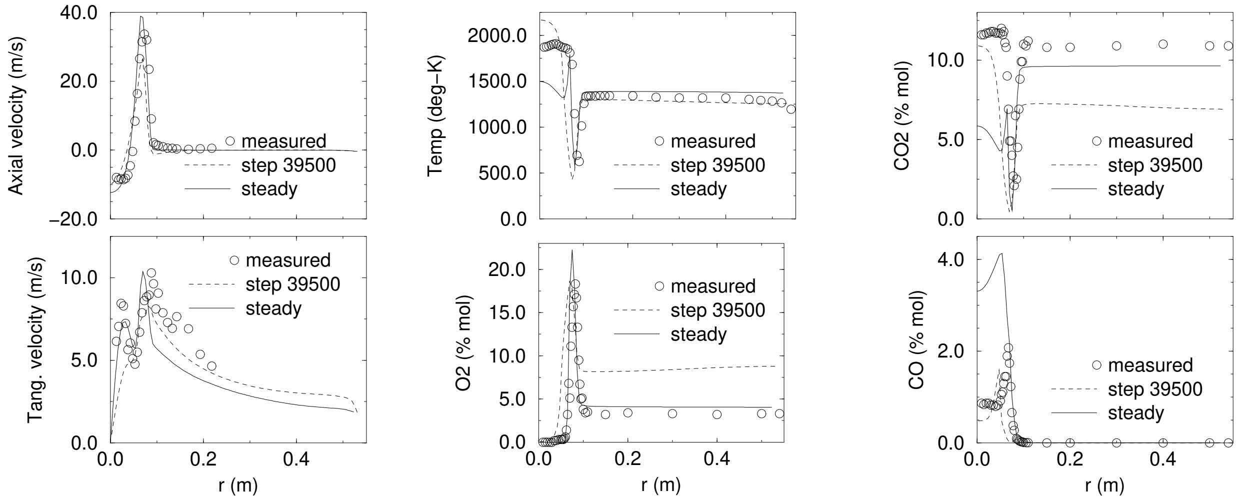

Figure 4: Radial profiles of velocity, temperature, and gas species mole fractions at 0.027m downstream of the burner throat.

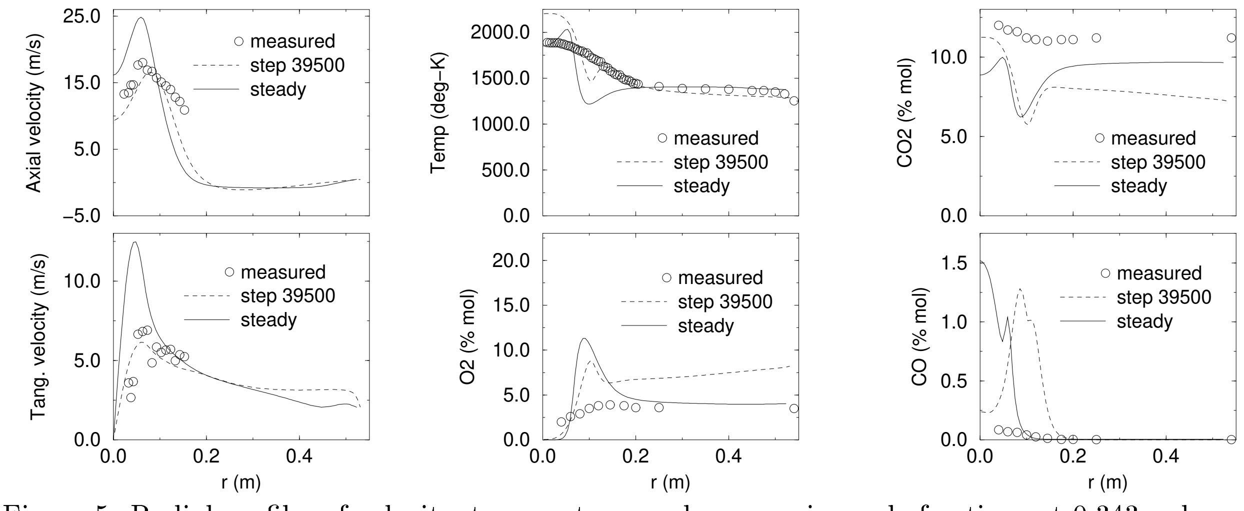

Figure 5: Radial profiles of velocity, temperature, and gas species mole fractions at 0.343m downstream of the burner throat.

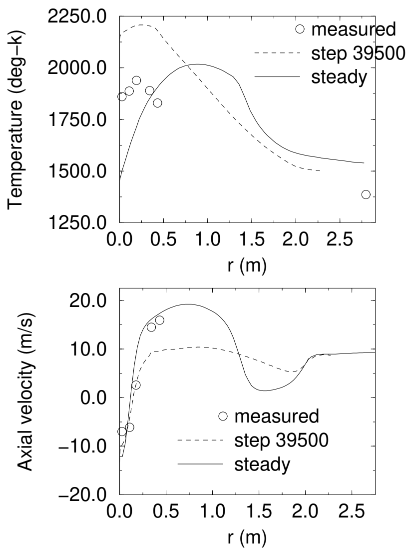

Figure 6: Measured and computed profiles of axial velocity and temperature along the burner centerline. The x-axis represents the distance downstream of the burner throat. The measured velocities are taken at 3mm off the centerline. The unsteady results represent the solution at $r = \Delta r/2 = 2.78$mm.

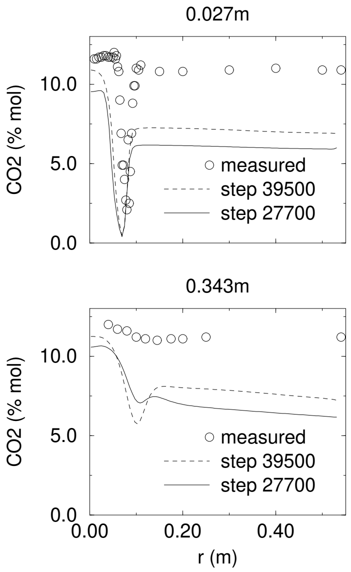

Figure 7: Measured and computed profiles of CO_2 mole fractions at 0.027m and 0.343m downstream of the burner throat.

intermixing of fuel and oxidizer is not the limiting process in oxidization were not accounted for.

The computed axial velocities along the centerline downstream of the burner throat are noticeably less than the measured values. We are uncertain of the cause of this numerical feature.

7 CONCLUSIONS

We have used a higher-order projection method for unsteady axisymmetric reacting flow to model natural gas combustion in a laboratory furnace. In general, the predictions compare favorably with the experimental data. Plausible explanations of discrepancies have been offered.

The method as described here is not well suited for efficiently computing steady or quasi-steady flows because the time step is limited by the CFL condition (11) and because a uniform grid is used. The use of an implicit, higher-order upwind scheme may overcome the first limitation. Incorporating the method into an adaptive mesh refinement [23] scheme would eliminate the inefficiencies of using a uniform grid. The authors are currently pursuing the second approach.

We note that the study here did not actually test the time dependent nature of the algorithm. Earlier results [24] suggest the methodology accelerates the solution too rapidly to steady state for it to be a reliable predictor of unsteady flow. We believe that the use of the $k-\epsilon$ model causes this acceleration. Testing the ability of the method to predict unsteady turbulent combustion will require the use of a turbulence model better suited to time-dependent flows.

8 NOMENCLATURE

$C_1, C_2,$	
$\sigma_k, \sigma_\epsilon$	constants used in the $k-\epsilon$ model
c_p	specific heat of the gas mixture
g	acceleration due to gravity
m_l	mass fraction of species l
μ_t	turbulent viscosity
mw_l	molecular weight of species l
mw_{mix}	molecular weight of the gas mixture
R_{ij}	turbulent stress tensor
τ	stress tensor
U	$(u,v)^T$

References

[1] R.B. Pember, A.S. Almgren, W.Y. Crutchfield, L.H. Howell, J.B. Bell, P. Colella, and V.E. Beckner. An embedded boundary method for the modeling of unsteady combustion in a gas-fired furnace. Fall Meeting, Western States Section of the Combustion Institute, 1995, WSS/CI 95F-165.

[2] K.C. Kaufman, W.A. Fiveland, A.A.F. Peters, and R. Weber. The BERL 300kW unstaged natural gas flames with a swirl-stabilized burner. Case 1: Hot-wall conditions. A benchmark problem for validating mathematical combustion models. Gas Research Institute, GRI Contract No. 5093-260-2729, November, 1994.

[3] K.C. Kaufman and W.A. Fiveland. Validation of industrial gas burner models using in-furnace laboratory measurements. In *Proceedings of the AFRC Fall International Symposium.* Monterey, CA, October 15-18, 1995.

[4] J.P Jessee and W.A. Fiveland. A non-orthogonal combustion model for natural gas flames. In *Proceedings of the Third International Conference on Combustion Technologies for a Clean Environment.* Lisbon, Portugal, July 3-6, 1995.

[5] R.G. Rehm and H.R. Baum. The equations of motion for thermally driven buoyant flows. *N.B.S.J.Res.*, 83:297–308, 1978.

[6] A. Majda and J.A. Sethian. The derivation and numerical solution of the equations for zero Mach number combustion. *Combust. Sci. Tech.*, 42:185–205, 1985.

[7] C.K. Westbrook and F.L. Dryer. Simplified reaction mechanisms for the oxidation of hydrocarbon fuels in flames. *Combust. Sci. Tech.*, 27:31–43, 1981.

[8] B.E. Launder and D.B. Spalding. The numerical computation of turbulent flows. *Comp. Meth. Appl. Mech. Eng.*, 3:269–289, 1974.

[9] R.W. Bilger. Turbulent diffusion flames. *Ann. Rev. Fluid Mech.*, 21:101–135, 1989.

[10] M. Frenklach, H. Wang, C.T. Bowman, R.K. Hanson, G.P. Smith, D.M. Golden, W.C. Gardiner, and V. Lissianski. An optimized kinetics model for natural gas combustion. 25th International Symposium on Combustion, Irvine, California, 1994, Work-In-Progress Poster Session 3, Number 26.

[11] J.B. Bell, P. Colella, and H.M. Glaz. A second-order projection method for the incompressible Navier-Stokes equations. *J. Comput. Phys.*, 85:257–283, 1989.

[12] A.S. Almgren, J.B. Bell, and W.G. Szymczak. A numerical method for the incompressible Navier-Stokes equations based on an approximate projection. *SIAM J. Sci. Comput.*, accepted for publication.

[13] L.S. Caretto, A.D. Gosman, S.V. Patankar, and D.B. Spalding. Two calculation procedures for steady, three-dimensional flows with recirculation. In *Proceedings of the Third International Conference on Numerical Methods in Fluid Mechanics.* Paris, France, July, 1972, Vol. II, p.60-68.

[14] D.G. Sloan, P.J. Smith, and L.D. Smoot. Modeling of swirl in turbulent flow systems. *Prog. Energy Combust. Sci.*, 12:163–250, 1986.

[15] A.S. Almgren, J.B. Bell, P. Colella, and T. Marthaler. Cartesian grid methods for incompressible flow in complex geometries. *SIAM J. Sci. Comput.*, accepted for publication.

[16] W.A. Fiveland. A discrete-ordinates method for predicting radiative heat transfer in axisymmetric enclosures. ASME Paper No. 82-HT-20, 1982.

[17] W. A. Fiveland. Discrete-ordinates solutions of the radiative transport equation for rectangular enclosures. *J. Heat Transfer*, 106:699–706, November 1984.

[18] E. E. Lewis and W. F. Miller, Jr. *Computational Methods of Neutron Transport.* American Nuclear Society, La Grange Park, IL, 1993.

[19] W.L. Briggs. *A Multigrid Tutorial.* SIAM, Philadelphia, PA, 1987.

[20] A. Sayre, N. Lallemant, J. Dugue, and R. Weber. Scaling characteristics of aerodynamics and low-NOx properties of industrial natural gas burners: The SCALING 400 study. Part IV: The 300kW BERL test results. Gas Research Institute, GRI Contract No. 5090-298-1977, 1994.

[21] R.B. Pember, J.B. Bell, P. Colella, W.Y. Crutchfield, and M.L. Welcome. An adaptive Cartesian grid method for unsteady compressible flow in irregular regions. *J. Comput. Phys.*, 120(2):278–304, 1995.

[22] W. Bartok and A.S. Sarofim. *Fossil Fuel Combustion: A Source Book*. Wiley-Interscience, 1991.

[23] A.S. Almgren, J.B. Bell, P. Colella, L.H. Howell, and M.L. Welcome. A high-resolution adaptive projection method for regional atmospheric modeling. In *Proceedings of the NGEMCOM Conference*. Sponsored by the U.S. EPA, August 7-9, 1995, Bay City, MI.

[24] R.B. Pember, A.S. Almgren, J.B. Bell, P. Colella, L.H. Howell, and M. Lai. A higher-order projection method for the simulation of unsteady turbulent nonpremixed combustion in an industrial burner. In *Proceedings of the 8th International Symposium on Transport Phenomena in Combustion*. San Francisco, CA, July 16-20, 1995.